

Materials Research Express



PAPER

Laser surface melting of γ -TiAl alloy: an experimental and numerical modeling study

RECEIVED
5 October 2018

REVISED
30 November 2018

ACCEPTED FOR PUBLICATION
8 January 2019

PUBLISHED
23 January 2019

Mallikarjuna Balichakra¹ , Srikanth Bontha^{1,3} , Prasad Krishna¹ and Vamsi Krishna Balla^{2,3}

¹ Department of Mechanical Engineering, National Institute of Technology Karnataka, Surathkal, Mangaluru-575 025, India

² Bioceramics and Coatings Division, CSIR-Central Glass and Ceramic Research Institute, 196 Raja S C Mullick Road, Kolkata-700 032, India

³ Authors to whom any correspondence should be addressed.

E-mail: srikanth.bonth@nitk.edu.in and vamsiballa@cgcri.res.in

Keywords: γ -TiAl Alloys, laser surface melting (LSM), melt pool dimensions, residual stress, thermomechanical finite element analysis

Abstract

The objective of present work is to study the evolution of thermal stresses during laser surface melting (LSM) of γ -TiAl alloy using experimental and numerical modeling approaches. LSM of γ -TiAl alloy samples were carried out at different processing conditions in a controlled atmosphere. Material characterization of the melted region was investigated using scanning electron microscope. It was found that fully lamellar microstructure was transformed into predominantly γ -TiAl with little amount of α_2 -Ti₃Al. A maximum improvement in hardness of over 72% was noticed in the melted region compared to that of the substrate. Three-dimensional thermomechanical finite element analysis of LSM of γ -TiAl alloy was carried out. Melt pool dimensions, temperature history, and residual stresses were predicted from the finite element models. Measured and predicted values of melt pool depth were in good agreement with a maximum error of 13.6% at $P = 400$ W and $V = 10$ mm s⁻¹. Predicted residual stress in the melted region exceeded the yield strength of γ -TiAl alloy and resulted in cracking of the melted region at all process conditions.

1. Introduction

Gamma TiAl (γ -TiAl) is an intermetallic alloy, exhibiting attractive properties such as low density, high corrosion and oxidation resistance at elevated temperatures. These unique attributes enable γ -TiAl alloys as a potential material for aerospace, biomedical, automotive, and power plant applications [1–3]. To produce efficient bonding and improvement in the surface properties of TiAl alloys, a fine-grain structure is required. In this regard, Laser Surface Melting (LSM) is one of the widely used surface modification techniques for tailoring surface properties such as fine microstructures, crystallographic texture, compositional homogenization, high corrosion and wear resistance. LSM is generally carried out in a controlled atmosphere to avoid oxidation of metals being processed [4–6]. In LSM process, a high-power laser beam moves along the surface of the metal substrate, melting metal without the addition of any filler material. Zielinski *et al* [7] carried out surface melting under cryogenic conditions. They concluded that at higher laser power, the depth of melting and hardness of the surface increased. In another study on LSM by Robinson *et al* [8] residual stresses were measured using x-ray diffraction technique in the melted region of samples. They reported that the remelted single tracks do not have cracks. However, cracks have been found in the multitrack overlapped samples due to the high tensile stresses in the melted region.

Several researchers used a combination of experimental and numerical modelling approaches to optimize LSM process parameters and have also studied the evolution of residual stresses during LSM of different alloys. It was reported that high temperatures and rapid cooling rates associated with LSM generate residual stresses which exceed the yield strength of the material leading to cracking [9–12]. Yilbas *et al* [13] carried out 3D thermomechanical finite element modelling of LSM of alumina and observed that high thermal gradients and cooling rates in the remelted region cause high Von Mises stress. They reported that cracks form in the remelted

region once the stress exceeds the yield strength of alumina. Further, it was reported [14] that the generation of high temperature in the vicinity of the surface leads to the high residual stress accumulation. In another study, Yilbas *et al* [15] investigated both the evolution of temperature and stresses during LSM of an aluminium composite using both experimental and numerical modeling approaches. LSM samples reveal crack-free surface due to self-annealing effect. The predicted temperatures using Finite Element Analysis (FEA) were validated with thermocouple measurements. In a recent study on laser surface treatment of IN718, it was reported that the higher hardness in the remelted region, is due to altered microstructure and high cooling rates. It was further reported that predicted Von Mises stress is highest at the location, where the highest temperature was recorded during irradiation [16].

Limited literature exists in the area of laser processing of TiAl alloys [17–23]. Wu *et al* [17] investigated the laser surface melting of TiAl alloy. They reported that LSM produces smaller grains which lead to the low-temperature bonding of TiAl components. In another study, Wu *et al* [18] examined the laser surface remelted and post heat-treated γ -TiAl alloy samples. They have reported ultrafine grain structure due to the structural transformation of the γ -TiAl alloy. Carcel *et al* [22] studied cladding of TiAl powder on $\text{Ti}_6\text{Al}_4\text{V}$ substrate, and it was reported that preheating of substrate reduced the chances of crack formation in the samples. In a recent study, Balla *et al* [23] reported that cracking of TiAl samples occurs during multi-layer deposition at most processing conditions due to high cooling rates and thermal gradients leading to the development of residual stresses. It can be concluded from a review of literature, that rapid solidification and high thermal gradients during laser processing lead to the generation of residual stresses which are in particular detrimental to successful processing of inherently brittle TiAl alloys. Hence there is a need to thoroughly understand the thermal behaviour during laser processing of TiAl alloys which is the focus of this work. At this time of reporting no literature has been found on numerical modeling of LSM of TiAl alloys for prediction of residual stress.

In the present study, an experimental and numerical investigation on LSM of γ -TiAl alloy were carried out. The surface melting of γ -TiAl samples were carried out using the Laser Engineered Net Shaping (LENS) machine. The samples were processed at powers of 200, 300 and 400 Watts at a constant velocity of 10 mm s^{-1} . The melted samples were characterized for melt pool dimensions, microstructure, and microhardness. A three-dimensional (3D) thermomechanical finite element analysis was performed to understand the thermal behaviour and residual stress evolution during LSM of a γ -TiAl alloy. The melt pool dimensions predicted from FEA were compared with experimental data. Further, the predicted stress distributions from the numerical models were used to understand the formation of cracks.

2. Materials and experimental approach

In the present work, LSM was carried out on a γ -TiAl plate that was fabricated using the Electron Beam Melting (EBM) process. The composition of the powder (at. %) of Al is 47.54–49.93, Cr is 1.64–2.00 and Nb is 1.88–2.11 and rest is Ti. LSM is carried out using the laser (500 W continuous wave ytterbium-doped fiber) system of the Laser Engineered Net Shaping (LENS), in a controlled atmosphere, different processing conditions were used to melt the samples and are presented in table 3. Laser energy density is calculated as [23]

$$E = \frac{P}{Vd} \quad (1)$$

Where E is the laser energy density in J/mm^2 , P is the laser power in Watts, V is the velocity in mm/s and d is the laser spot diameter in mm. Once the LSM was done, phase analysis was carried out using x-ray diffraction on the substrate and melted region. Then the samples were prepared for microstructural characterization and microhardness measurement. The etching of polished samples was carried out using Kroll's reagent which comprises 300 ml H_2O , 100 ml HF, and 100 ml HNO_3 . Samples were then examined using a scanning electron microscope (JEOL JSM 6380LA operating at 20 kV) to measure the melt pool depth and analyse microstructural features of both the melted region and substrate. Finally, Vickers microhardness measurements were performed on the melted region using a load of 200 g applied for 15 s and an average of 10 measurements was reported.

3. Numerical modeling approach

The transient thermal analysis was first performed followed by mechanical analysis. The temperatures from the transient thermal analysis were exported to the mechanical analysis i.e., the temperature history is applied as a load during mechanical analysis.

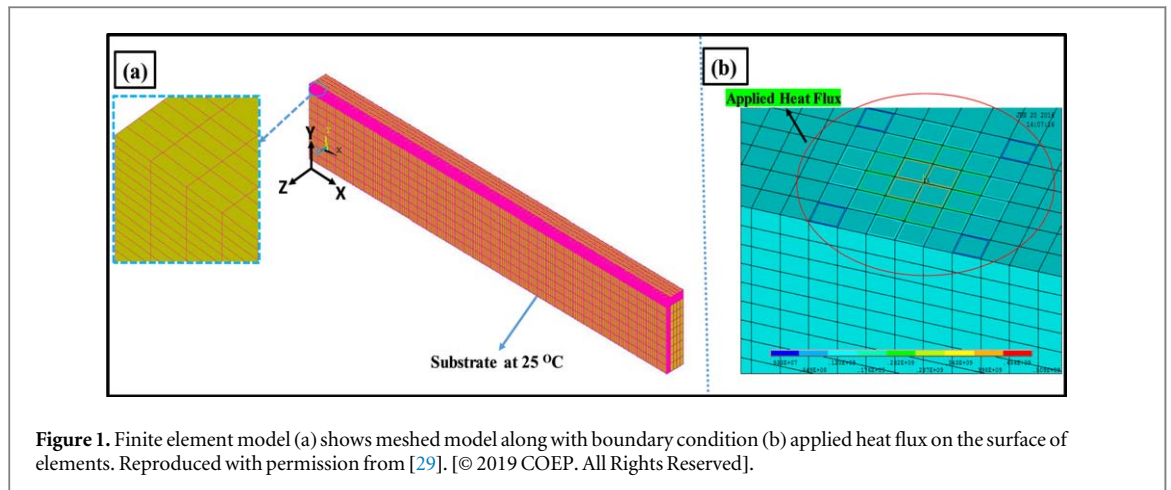


Figure 1. Finite element model (a) shows meshed model along with boundary condition (b) applied heat flux on the surface of elements. Reproduced with permission from [29]. [© 2019 COEP. All Rights Reserved].

Table 1. Thermophysical properties [26].

Temperature °C	25	127	327	527	727	927	1460	1534
Density Kg/m ³	3900	—	3879	—	3853	3840	—	3800
Specific heat J/KgK	610	635	—	695	—	—	1060.4 ^a	—
Thermal conductivity W/m K	10.5	—	—	21	—	—	—	28

^a Modified specific heat at the melting temperature to include effect of latent heat.

3.1. Geometry and mesh attributes

The commercially available Finite Element Analysis (FEA) package ANSYS was used to simulate the LSM process. In the FE model, the dimensions of the plate considered were 50 mm (length) × 8.6 mm (width) × 2 mm (thickness). In the meshed model, solid 70 and solid 185 elements were used for thermal and mechanical analysis respectively. The model consists of 56 000 elements and 64 119 nodes. Highly refined mesh with an element size of 250 μm length × 50 μm width × 83 μm thickness (enlarged view of figure 1(a)) was used along the laser travel direction (i.e. along with the *x*-axis). The temperature of the bottom surface of the substrate is fixed at 25 °C, while all other faces are insulated ($q = 0$).

Assumptions made in numerical modelling include:

- Convection and radiation are neglected as the predominant mode of heat transfer in LSM is conduction [24].
- Marangoni effect in the melt pool was not considered.
- The laser is modelled as a heat source with a Gaussian distribution of power.

3.2. Material properties

The thermophysical properties of γ -TiAl alloy such as density, conductivity, specific heat were inputs to the model as a function of temperature. The thermophysical properties are presented in table 1. Also, the latent heat of fusion during melting was taken into consideration by modifying the specific heat at the melting temperature using the following equation [25].

$$C_p^* = C_p + \frac{L}{T_m - T_0} \quad (2)$$

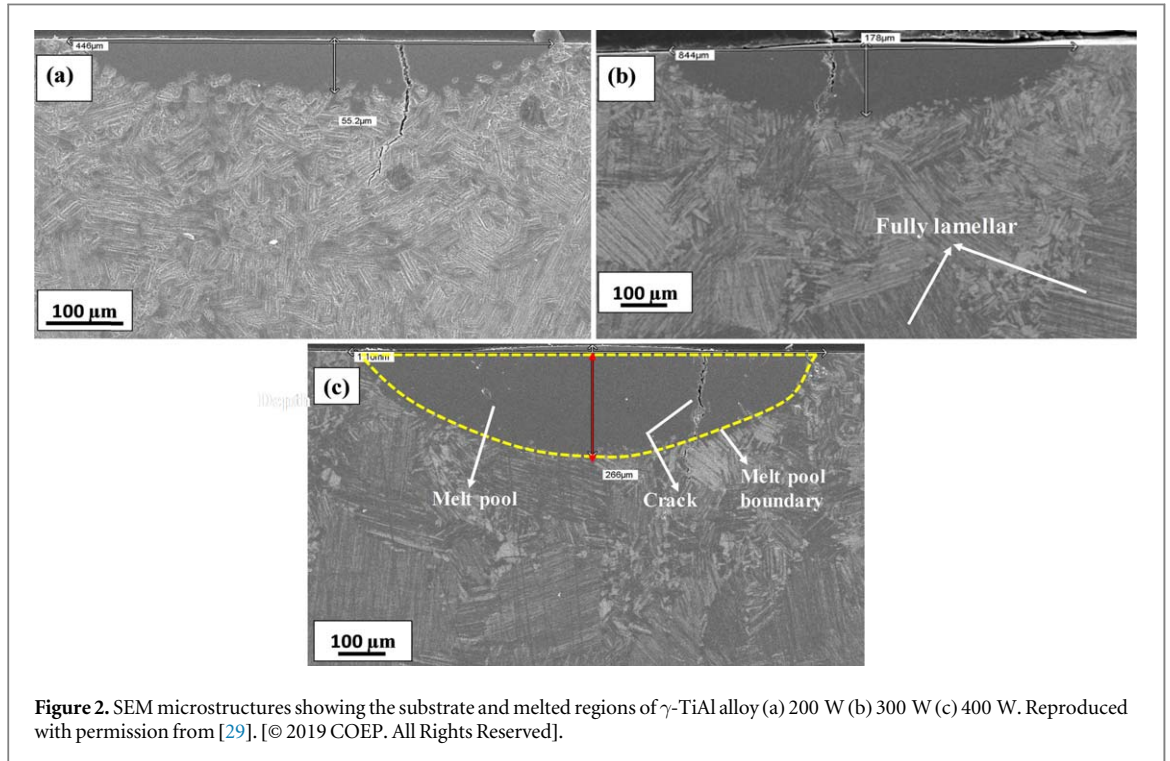
where C_p^* is the modified specific heat at melting temperature, C_p is the actual specific heat at melting temperature, L is the latent heat of fusion, T_m is the liquidus temperature of the γ -TiAl alloy and T_0 is the initial temperature of the substrate which is 25 °C. Mechanical properties with linear isotropic hardening model were used in structural analysis the values of which are provided in table 2.

3.3. Heat source model

The finite element model simulates the LSM process as movement of heat source from the left to the right end of the model. The laser beam is modelled as a heat source with Gaussian distribution as given by [28].

Table 2. Properties used in structural analysis [27].

Temperature °C	25	150	300	450	600	900
Young's modulus GPa	172	—	162	—	153	—
Yield strength N/m ²	359×10^6	—	358×10^6	—	—	259×10^6
Thermal expansion 10^{-6}K^{-1}	11	11.7	12.3	—	—	15
Poisons ratio	0.22	0.22	0.22	—	—	—
Tangent modulus MPa	377×10^6	—	376×10^6	—	—	—

**Figure 2.** SEM microstructures showing the substrate and melted regions of γ -TiAl alloy (a) 200 W (b) 300 W (c) 400 W. Reproduced with permission from [29]. [© 2019 COEP. All Rights Reserved].

$$I(x, y) = \frac{2 \alpha Q}{\pi r^2} e^{-2 \frac{x^2 + y^2}{r^2}} \quad (3)$$

Where I is the heat flux in J/mm^2 , α is the laser absorption coefficient, Q is the laser power in Watts, r is the radius of the laser beam in mm and (x, y) are the variables which specify the distance from the center of the laser beam. The laser beam completes a single pass by traversing from the left to right end of the model with a velocity V . The movement of the laser beam was taken into account using a moving coordinate system. Heat flux was applied using equation (3) over a $0.5 \times 0.5 \text{ mm}^2$ surface area of the elements as shown in figure 1(b).

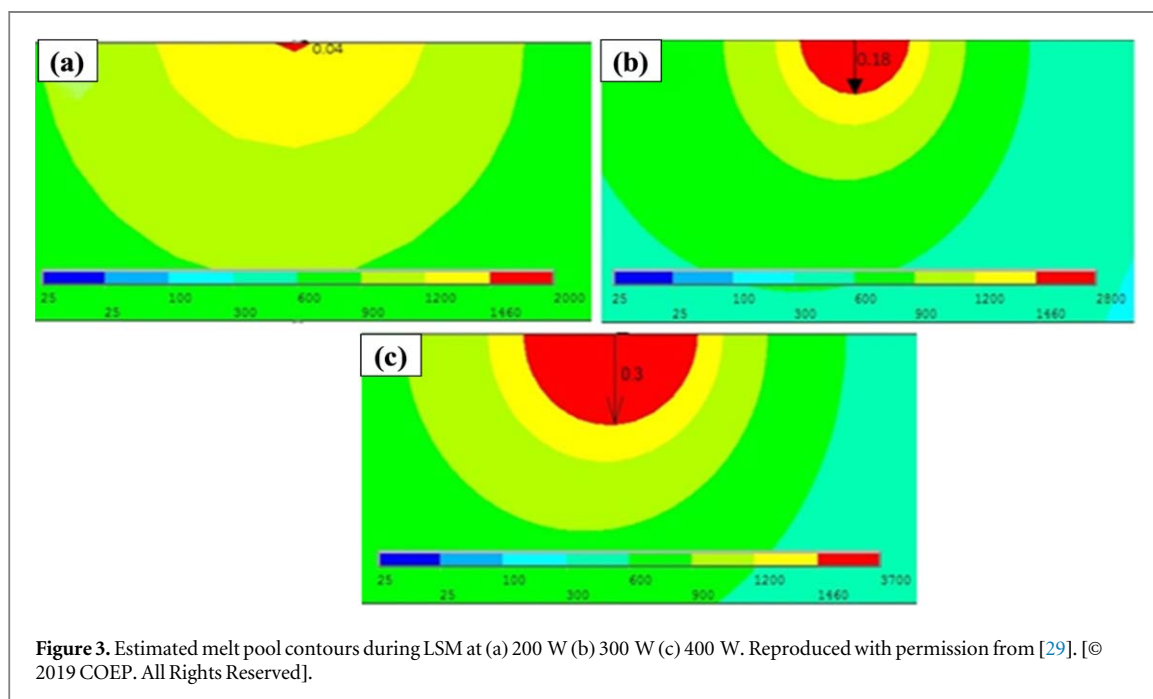
4. Results and discussion

4.1. Microstructural and melt pool analysis of LSM samples

Figure 2 shows the microstructures of the substrate and melted region of γ -TiAl alloy samples processed at different laser powers. The substrate exhibited fully lamellar microstructure consisting of alternating γ -TiAl and α_2 -Ti₃Al plates stacking up into lamellas. It was studied that this kind of similar lamellar structure was found to be more ductile than the equiaxed microstructure. The microstructure of the melted region showed single phase and appears to be massive γ phase. The formation of single phase in this region is attributed to the rapid cooling rates experienced by the material during LSM. The LSM regions of the sample also showed cracks under all processing conditions. Further, the cracks appear to have propagated from the surface of the melt pool into the substrate. Maximum crack length along the melt pool cross section was measured to be $600 \mu\text{m}$ in the samples processed with 400 W and 10 mm s^{-1} . The results indicate that the crack depth increases with increasing power at constant velocity. This is attributed to the deeper melt pools and stress fields present in the melted regions formed during LSM at high laser power. Further, the cracking indicates that the developed residual stresses are tensile in nature and are exceeding the yield strength of the material. The melt pool dimensions such as depth and length have increased as the laser power increases from 200 W to 400 W.

Table 3. Process conditions, melt pool dimensions and microhardness values of the melted region. Reproduced with permission from [29]. [© 2019 COEP. All Rights Reserved].

Power (W)	Velocity (mm s^{-1})	Laser energy density (J mm^{-2})	Melt pool length (μm)	Melt pool depth (μm)	Hardness (HV)
200	10	40	476 ± 42	65 ± 14	515 ± 9
300	10	60	850 ± 8	180 ± 4	508 ± 15
400	10	80	1120 ± 11	259 ± 7	493 ± 11



The variation in the hardness of the melted regions are presented in table 3. The hardness of the substrate was measured to be 300 ± 15 HV. However, the hardness of the alloy increases significantly after LSM. The hardness of LSM region ranged between 493 to 515 HV and laser power was found to have little influence. This improvement of hardness can be attributed to the microstructural changes such as phase transformations and refined microstructural features as a result of rapid cooling rates. The microstructure changes from lamellar (substrate) to massive γ - formation in the melt pool during LSM. However, processing conditions which were used for LSM samples have no significant effect on hardness primarily due to similar microstructural features exhibited in the melt pool of the samples processed at different laser processing parameters.

4.2. Thermomechanical analysis of LSM process

4.2.1. Melt pool dimensions

Figure 3 presents the temperature contours in the melted region. The red colored region in these contours indicates the melt pool region i.e., region where the temperature is greater than the liquidus temperature of γ -TiAl alloy. The melt pool depth and length were measured from these contours and were compared with experimentally determined dimensions. From figure 4(a) it is evident that measured and predicted values of melt pool depth are in good agreement with a maximum error of 13.6% at $P = 400$ W and $V = 10$ mm s^{-1} . Further, it can be seen that as the laser power is increased from 200 to 400 W, the melt pool depth increases from 65 to 259 μm . Figure 4(b) presents the experimental and numerical predictions of melt pool length as a function of laser power. From the plot, it is evident that the modelling results agree with the trend of experimental data. However, the measured melt pool lengths were higher than the predicted values. The reasons for this discrepancy can be attributed to the assumptions that were made in thermomechanical analysis.

4.2.2. Temperature fields

The temperature distribution in the melt pool along the width direction is presented in figure 5(a). These temperatures were extracted at the center of the melt pool. For all laser powers, it can be observed that temperature decreases with increase in the width. The maximum temperature occur at the location of maximum applied heat flux in accordance with the heat source model represented by equation (3). Applied heat flux on the surface of the solid sample is shown in figure 1(b). As the laser power is increased from 200 to 400 W, the peak

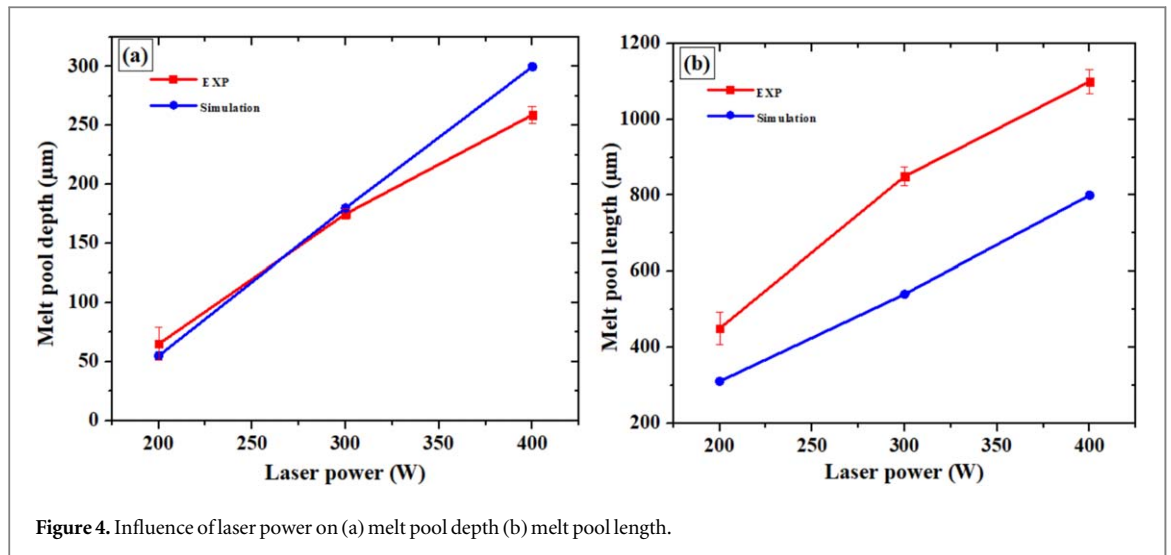


Figure 4. Influence of laser power on (a) melt pool depth (b) melt pool length.

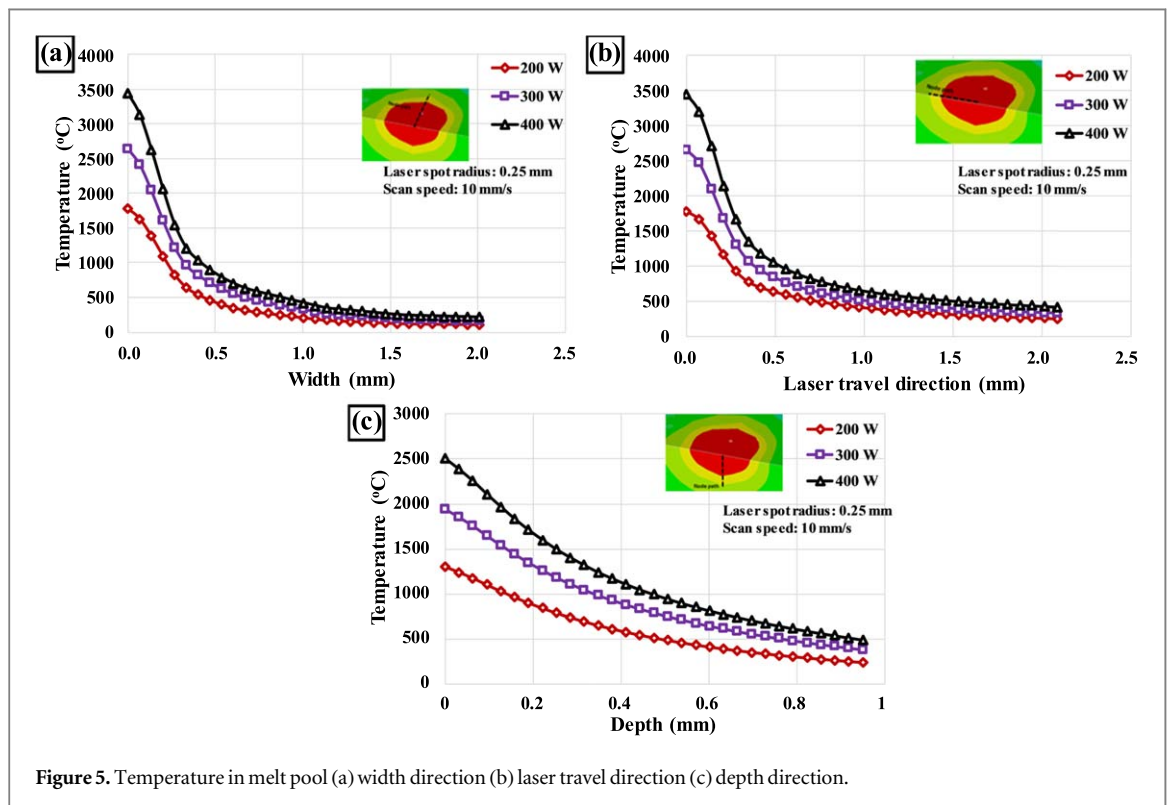


Figure 5. Temperature in melt pool (a) width direction (b) laser travel direction (c) depth direction.

intensity of heat flux was found to increase from $89\,061\text{ W m}^{-2}$, to $180\,272\text{ W m}^{-2}$. It is observed that as the laser power increases, heat flux increased at the center of the laser beam. This heat flux diminishes by $1/e^2$ as it radially moves outward from the center of the laser beam. Therefore, peak temperature and their profile changed in accordance with the irradiance intensity on the surface of the solid samples along width and longitudinal directions.

The distribution of temperature along the longitudinal direction is shown in figure 5(b). A steep temperature change is noticed in this direction as compared to the other two directions. The temperature becomes steeper as the laser power is increased from 200 W to 400 W at the surface. This gradient in temperature distribution is mainly the higher energy density found on the surface rather than the subsurface. The temperature distributions along the depth direction are presented in figure 5(c). Temperatures were extracted at the center of the melt pool starting from the surface through a depth of $1000\ \mu\text{m}$. This depth of $1000\ \mu\text{m}$ encompasses the molten pool as well as the HAZ. It is clearly evident from these plots that for all laser powers, temperatures decreased rapidly from the melt pool surface to the substrate. Further, increasing laser power at constant velocity results in higher

Table 4. Cooling rates, temperature and thermal gradients at melt pool surface.

Velocity 10 mm s ⁻¹ Power (W)	Cooling rates °C/s (Melt pool surface)	Temperature (°C)		Thermal gradients (°C/m)	
		Middle (Region B)	Right end (Region C)	Middle (Region B)	Right end (Region C)
200	6.0×10^5	1774	1993	2.60×10^6	2.67×10^6
300	3.12×10^5	2645	3061	3.82×10^6	4.08×10^6
400	1.25×10^5	3436	3999	5.09×10^6	5.45×10^6

temperature gradients. It is evident from the figure 5(c) that the maximum temperature at the melt pool surface along the depth direction is 1464 °C, 2000 °C and 2500 °C for 200 W, 300 W, and 400 W respectively.

4.2.3. Cooling rate

The cooling rates experienced by the material during LSM were extracted from the transient thermal analysis on the melt pool surface. The liquidus and solidus temperatures of the TiAl alloy are 1460 °C and 1440 °C respectively. In this narrow temperature range, the variation of temperature with time is assumed to be linear. The cooling rate at the onset of solidification is given by the equation (4) [24].

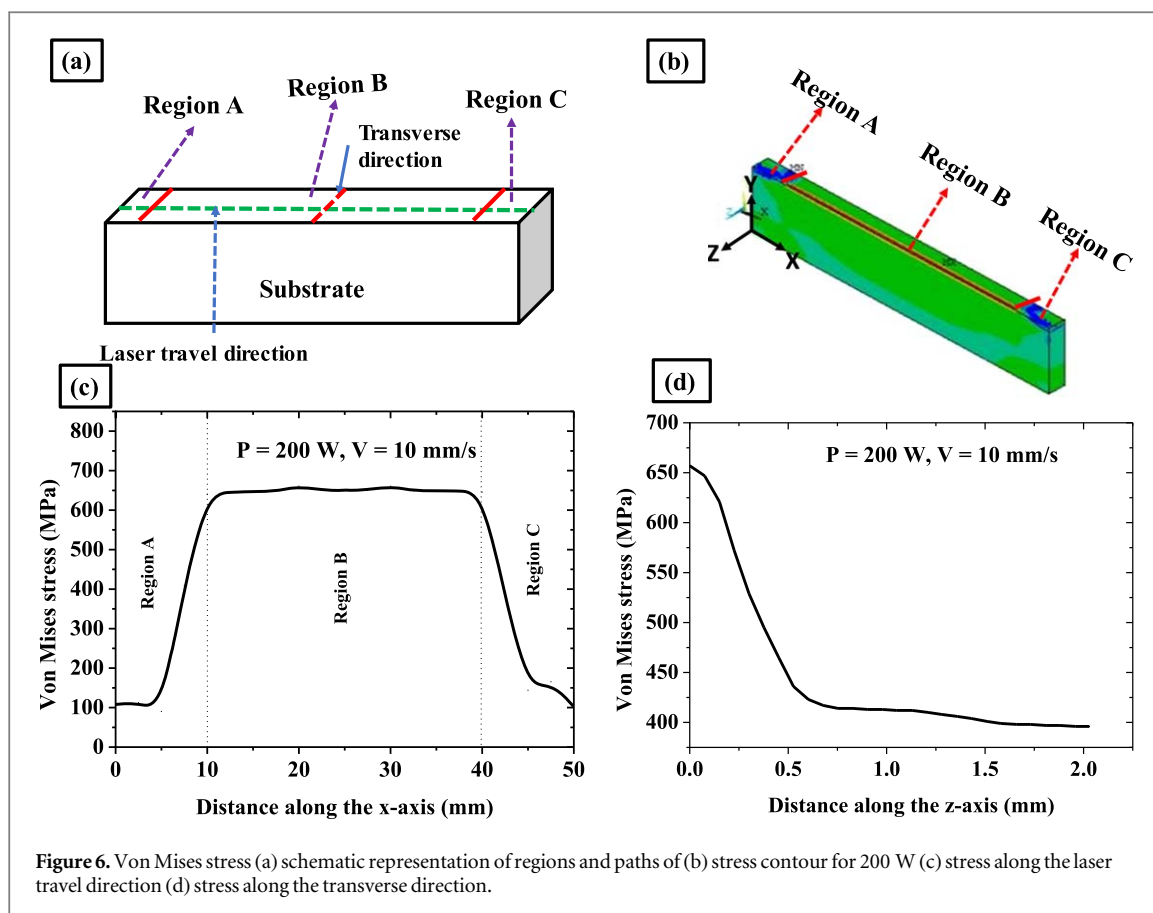
$$\frac{\partial T}{\partial t} = \left| \frac{T_s - T_L}{t_s - t_l} \right| \quad (4)$$

where T_L and T_s are the liquidus and solidus temperatures attained at times t_l and t_s respectively. To extract the cooling rates, time versus temperature data was used on the surface of the melt pool. The maximum cooling rate was observed at surface and minimum at the bottom of the melt pool. Cooling rates thus estimated for the three powers are presented in table 4. The cooling rates decreased from 6.0×10^5 °C/s to 1.25×10^5 °C/s with increase in power from 200 W to 400 W. This shows that at laser power 400 W increases the thermal energy in the irradiated region. This resulted into, large thermal gradients and low cooling rates in irradiated region which is processed at 400 W. These high cooling rates are found to have a direct influence on the microstructures, hardness, and cracks observed in these samples. For example, high cooling rates results in refined microstructures leading to increase in the hardness. At the same time, the rapid cooling rates could generate excessive residual stresses [22] in the melted region and can develop cracks in the melt pool, as shown in figure 2. Therefore, prediction of cooling rates during melting enables better control of microstructures and cracking propensity.

4.2.4. Von Mises stresses

The rapid cooling rates can generate large amount of stresses during solidification, which can lead to cracking. The schematic representation of regions and stress extraction path is shown in figure 6(a). Von Mises stress contour for 200 W is shown in figure 6(b). The maximum stress was found in the mid-top surface of the substrate and minimum stress was found at either end of the substrate. The stress distribution at room temperature along the x -axis is shown in figure 6(c). The stress plot is divided into three regions i.e., Region A is left end of the substrate; Region B is the middle or core of the substrate and Region C is the right end of the substrate. It can be seen that the stress gradually reduced at regions A and C, while uniform stress distribution was exhibited in region B due to the anisotropic thermal gradients in these regions. Similar stress distribution has been reported by Yilbas *et al* [13] in laser surface melted alumina. Thermal gradients at the surface of the melt pool in the three regions are summarized in table 4, which shows that thermal stress is relieved in regions A and C, due to large thermal gradients. Highest Von Mises stresses at region B is due to the steep thermal gradients along the x -axis at the surface vicinity. It is understandable that the developed residual stress should not exceed the yield strength of the material to prevent cracking. However, the maximum stress in the melted region was found to be 596 MPa (for 200 W) exceeding the yield strength of the material (400 MPa) and therefore resulted in cracking. Further, similar stress behavior was observed in the samples processed at 300 W and 400 W power. However, with increasing laser power from 200 W to 400 W, the magnitude of stress also increased from 596 MPa to 835 MPa. Since the induced stresses exceeded the yield strength of the present material all samples showed microcracks, as shown in figure 2.

The Von Mises stress for 200 W at room temperature along the transverse direction is shown in figure 6(d). The stress decreased while moving away from the laser irradiation spot which is evident from figure 5(a). The stress variation followed Gaussian heat flux distribution, i.e., bell shape at the laser irradiation region while a constant value of stress in the rest of the region. Also, the magnitude of stress developed in the transverse direction exceeded yield strength of γ -TiAl alloys. Hence, microcracks is also found along the transverse direction as well.



5. Conclusions

The current work focuses on experimental and numerical modelling study of laser surface melting of γ -TiAl alloy. Following conclusions were drawn from the present study:

- Microstructure of the substrate was fully lamellar and transformed to predominantly γ -TiAl with little traces of α_2 -Ti₃Al phases after LSM.
- Hardness improved in the melted region from 300 ± 15 HV to 515 ± 9 HV due to phase transformation and higher cooling rates.
- As the laser power increased from 200 to 400 W melt pool dimensions also increased. The measured and predicted values of melt pool depth were in good agreement with a maximum error of 13.6%.
- Microcracks were observed in all melted regions due to the high tensile stress in these regions which exceeds the yield strength of the material.
- Maximum Von Mises stress was predicted along the laser travel direction due to high thermal gradients.
- Predicted Von Mises stress of 596 MPa exceeded the yield strength of γ -TiAl alloys, justifying the formation of cracks in the melt pool region.

ORCID iDs

Mallikarjuna Balichakra <https://orcid.org/0000-0001-5598-0219>

Srikanth Bontha <https://orcid.org/0000-0002-8803-6774>

References

- [1] Appel F and Paul DH 2011 *Gamma Titanium Aluminide Alloys: Science and Technology* vol 12, 69469 (Weinheim, Germany: Wiley-VCH Verlag GmbH & Co. KGaA)
- [2] Bewlay B P, Nag S, Suzuki A and Weimer MJ 2016 TiAl alloys in commercial aircraft engines *Mater. High Temp.* **33** 549–59

- [3] Mohammad A, Al-Ahmari A M, Balla V K, Das M, Datta S, Yadav D and Janaki Ram G D 2017 *In vitro* wear, corrosion and biocompatibility of electron beam melted γ -TiAl Mater. Des. **133** 186–94
- [4] Rakesh K R, Bontha S, Ramesh M R, Arya S B and Das M 2018 Laser surface modification of Mg–Zn–Gd alloy : microstructural, wettability and *in vitro* degradation aspects Mater. Res. Express **5** 126502
- [5] Liu C, Liang J, Zhou J, Wang L and Li Q 2015 Effect of laser surface melting on microstructure and corrosion characteristics of AM60B magnesium alloy Appl. Surf. Sci. **343** 133–40
- [6] Yilbaş B S, Şahin A Z, Sami M, Çoban A and Bozdoğan R 1995 Study into laser heating of Ti₁₄Al₂₁Nb alloy to improve properties Opt. Lasers Eng. **23** 53–64
- [7] Zielinska A, Jazdzewska M and Narozniak-luksza W S A 2006 Surface structure and properties of Ti₆Al₄V alloy laser melted at cryogenic conditions J. Achiev. Mater. Manuf. Eng. **18** 423–6
- [8] Robinson J M, Brussel B A V, De H J T M and Reed R C 1996 X-ray measurement of residual stresses in laser surface melted Ti-6Al-4V alloy Mater. Sci. Eng. **208** 143–7
- [9] Labudovic M, Hu D and Kovacevic R 2000 Three-dimensional finite element modelling of laser surface modification Proc. Inst. Mech. Eng. Part B J. Eng. Manuf. **214** 683–92
- [10] Ziaja W 2009 Finite element modelling of the fracture behaviour of surface treated Ti-6Al-4V alloy Comput. Mater. Sci. Surf. Eng. **1** 53–60
- [11] Rubino F, Astarita A and Carlone P 2018 Thermo-mechanical finite element modeling of the laser treatment of titanium cold-sprayed coatings Coatings **8** 219
- [12] Telrandhe S V, Bhagyaraj J, Mishra S and Karagadde S 2018 A new approach to control and optimize the laser surface heat treatment of materials J. Mater. Process. Technol. **262** 492–502
- [13] Yilbas B S, Karatas C, Arif A F M and Abdul Aleem B J 2011 Laser control melting of alumina surfaces and thermal stress analysis Opt. Laser Technol. **43** 858–65
- [14] Yilbas B S, Akhtar S S and Karatas C 2011 Laser gas assisted melting of preprepared alumina surface including TiC particles at surface Surf. Eng. **27** 470–6
- [15] Yilbas B S, Akhtar S S, Karatas C, Ali H, Boran K, Khaled M, Al-Aqeeli N and Aleem A B J 2016 Laser treatment of aluminum composite and investigation of thermal stress field Int. J. Adv. Manuf. Technol. **86** 3547–61
- [16] Yilbas B S, Akhtar S S and Karatas C 2010 Laser surface treatment of inconel 718 alloy: thermal stress analysis Opt. Lasers Eng. **48** 740–9
- [17] Wu G Q and Huang Z 2003 Weldability and microstructure of laser-surface-remelted TiAl intermetallic alloy Mater. Sci. Eng. A **345** 286–92
- [18] Wu G Q, Luo G X, Huang Z and Ruan Z J 2006 Dendritic structural transformation of laser surface remelted γ -TiAl based alloy during post-heat treatment Mater. Lett. **60** 406–9
- [19] Zhang X D, Brice C, Mahaffey D W, Zhang H, Schwendner K, Evans D J and Fraser H L 2001 Characterization of laser-deposited TiAl alloys Scr. Mater. **44** 2419–24
- [20] Srivastava D 2002 Microstructural characterization of the γ -TiAl alloy samples fabricated by direct laser fabrication rapid prototype technique Bull. Mater. Sci. **25** 619–33
- [21] Qu H P, Li P, Zhang S Q, Li A and Wang H M 2009 The effects of heat treatment on the microstructure and mechanical property of laser melting deposition γ -TiAl intermetallic alloys Mater. Des. **31** 2201–10
- [22] Carcel B, Serrano A, Zambrano J, Amigo V and Carcel A C 2014 Laser cladding of TiAl intermetallic alloy on Ti₆Al₄V. Process optimization and properties Phys. Procedia **56** 284–93
- [23] Balla V K, Das M and Mohammad A 2016 Additive manufacturing of γ -TiAl: processing, microstructure, and properties Adv. Eng. Mater. **18** 1–8
- [24] Bontha S, Klingbeil N W, Kobryn P A and Fraser H L 2006 Thermal process maps for predicting solidification microstructure in laser fabrication of thin-wall structures J. Mater. Process. Technol. **178** 135–42
- [25] Fallah V, Alimardani M, Corbin S F and Khajepour A 2011 Temporal development of melt-pool morphology and clad geometry in laser powder deposition Comput. Mater. Sci. **50** 2124–34
- [26] Sung S Y and Kim Y J 2006 Modeling of titanium aluminides turbo-charger casting Intermetallics **15** 468–74
- [27] Yan L, Li W, Chen X, Zhang Y, Newkirk J, Liou F and Dietrich D 2016 Simulation of cooling rate effects on Ti-48Al-2Cr-2Nb crack formation in direct laser deposition Proc. 27th Annu. Int. Solid Free. Fabr. Symp.—An Addit. Manuf. Conf vol 69, pp 586–91
- [28] Fu C H and Guo Y B 2014 Three-dimensional temperature gradient mechanism in selective laser melting of Ti-6Al-4V J. Manuf. Sci. Eng. **136** 061004 -1
- [29] Mallikarjuna B, Krishna P, Balla V K, Das M and Bontha S 2016 Understanding thermal behavior in laser processing of titanium aluminide alloys Proc. 6th Int. & 27th All India Manuf. Technol. Des. Res. Conf. pp 73–7